Advantages of the frequency-conversion technique in quantum interference

Chen Yang,* Su-Jian Niu,* Zhi-Yuan Zhou,† Yan Li, Yin-Hai Li, Zheng Ge, Ming-Yuan Gao, Zhao-Qi-Zhi Han, Ren-Hui Chen, Guang-Can Guo, and Bao-Sen Shi‡

CAS Key Laboratory of Quantum Information and Synergetic Innovation Center of Quantum Information & Quantum Physics, University of Science and Technology of China, Hefei, Anhui 230026, China

(Received 15 March 2022; accepted 6 June 2022; published 21 June 2022)

Hong-Ou-Mandel (HOM) interference is a key phenomenon for understanding quantum interference and a basic tool for quantum information and metrological applications. By introducing the nonlinear frequency-conversion (NFC) technique into HOM interferometers, more phenomena could be found and more functions could be developed. Here, tunable quantum spatial beating is observed in a HOM interferometer based on the postfilter scheme, where two NFC modules function as tunable band-pass filters. Degenerate IR photon pairs at 1079.00 nm are generated based on the noncritical phase-matching spontaneous parametric down-conversion process and are up-converted to the visible band around 633.40 nm by the NFC modules before the detectors. We show that in addition to the filtering effect, the NFC can also improve the photon detection efficiency based on silicon avalanched detector, increasing the coherence length, and therefore improving the heralding efficiency and visibility. Our results demonstrate the advantages of the NFC technique in HOM interference, which could also be generalized to other quantum interference.

DOI: 10.1103/PhysRevA.105.063715

I. INTRODUCTION

Hong-Ou-Mandel (HOM) interference, discovered in 1987 [1], is not only used in a wide variety of applications in quantum optics and quantum information [2–6], but is also used in interferometry; being similar to a single-photon interferometer, the HOM interferometer is a powerful tool for measurement of optical delays between different paths [7]. However, unlike the single-photon interference, HOM interference is not affected by the relative phase between the two photons; therefore, it does not require a complex phase-stable feedback system. The state-of-the-art HOM interferometer has achieved few-attosecond (or nanometer path length) scale resolutions [8]. Besides, HOM interference is also used in quantum optical coherence tomography [9], automatic cancellation of even-order dispersion [10], and characterizing dispersion and absorption [11–14].

In 1988, using the same optical setup as the HOM interferometer, Ou and Mandel observed a spatial quantum beating phenomenon by inserting two band-pass filters with a nonoverlapping center frequency before two detectors [15]. In 2009, Ramelow *et al.* built a discrete frequency-entanglement source and the quantum beat note was observed [16]. From then on, the beat note became a character of the discrete frequency entanglement [17–20], from which the photon bandwidth and the frequency spacing can be deduced. Recently, Chen *et al.* demonstrated that the biphoton beat note based on the HOM interferometer with discrete frequency entanglement can be used for measurement and achieve great precision, where the precision is determined by the separation of center frequencies of the state [21]; their work significantly facilitates the use of the spatial beat note for quantum sensing. Since the HOM interference of the continuous frequency-entanglement state with postspectrally selective filtering has the same phenomenon as that of discrete frequency entanglement, it can also be used in the high timing resolution interferometry; comparing the two schemes, the latter has a significant advantage that the separation of center frequencies is tunable based on the tunable temperature of the crystal, while in the former scheme, the center frequency of a filter is usually not tunable. However, because the former scheme has the advantage that the setup for preparing the discrete frequency-entanglement state is not required, it is also a candidate scheme in HOM interferometry. Here, we introduce a special tunable filter to realize the postfiltering HOM scheme and make the frequency spacing tunable; moreover, the special filter can benefit the interference results from other aspects.

The tunable filter is played by the nonlinear frequency-conversion (NFC) module, which is a relatively mature technique that can change the frequency of an optical quantum state without changing its nonclassical properties. It is usually based on the three-wave mixing process based on a second-order nonlinear crystal, where the sum-frequency generation (SFG) and the difference-frequency generation (DFG) can be used in frequency up-conversion and down-conversion, respectively. The NFC has been used to convert the frequency of entanglement states for quantum communication [22,23], NOON states for quantum metrology [24], and single photons carrying imaging information [25]. For quantum communication, the NFC is used as a quantum interface to link the fiber and the quantum memory; for quantum metrology, the NFC can help to prepare a NOON state with a shorter wavelength

*These authors contributed equally to this work.
†zyzhouphy@ustc.edu.cn
‡drshi@ustc.edu.cn

 ©2022 American Physical Society

and therefore improve the resolution; for quantum imaging, the NFC enables the visible charge-coupled device (CCD) to detect the IR imaging. In this work, we fully demonstrate the advantages of the NFC in quantum interference based on a HOM interferometer and the beat note interference phenomenon.

In our experiment, we modify the original experiment in Ref. [15] and the narrow-band filters are replaced by two SFG modules. The photons are prepared by the degenerate spontaneous parametric down-conversion (SPDC) process in a potassium titanyl phosphate (KTP) crystal with a type-II noncritical phase matching [26]. Because of no periodic poling and no walk-off effect, the crystal with noncritical phase matching can have a larger dimension compared to the crystals with angle phase matching or quasi–phase matching; therefore, it has relatively high efficiency and is a promising candidate for experiments of correlated imaging [27]. However, the disadvantage of noncritical phase matching is that the wavelength cannot be designed flexibly compared to quasi–phase matching. The first advantage of the NFC is to convert the prepared photons to any wave band for a certain reason; for example, in our previous work, we prepared a NOON state with a shorter wavelength than the wavelength of the pump photons [28]. In this experiment, we focus on the other two advantages of the NFC: On the one hand, the SFG module plays the role of a tunable narrow-band filter; on the other hand, it can convert the infrared photons into the visible band. Usually, the quantum efficiency of visible detectors is much higher than infrared detectors such as an AsGaIn avalanched single-photon detector and the latter also suffer from low speed, high cost, high readout noise, and more rigorous cooling attachment requirements. Moreover, the detection efficiency of a silicon avalanched single-photon detector is below 2%, around 1079 nm. A visible detector with the aid of high-efficiency SFG can significantly improve the efficiency of infrared detection, around 1079 nm, and therefore improve the heralding efficiency. In addition, the filtering effect can increase the coherence length and optimize the superposition of the photons' spectra; therefore, the interference visibility can also be improved significantly. In a common HOM interferometer, one should try to reduce the coherence length to obtain a high sensitivity limit [8]; however, in the spatial beating experiment, the sensitivity is not limited by the coherence length [21] and one could still increase the coherence length to obtain a large measurement range.

II. METHODS

A flow chart of the experimental setup is shown in Fig. 1. Except for the SPDC process, three SFG modules are included: SFG0 provides the pump beam for the SPDC, SFG1 and SFG2 are used to implement frequency up-conversion, and the systems are linked by single-mode fibers. The width of the signal and idler photons' spectra are much wider than the acceptance bandwidth of SFG1 and SFG2. Therefore, SFG1 and SFG2 also act as narrow-band filters and we assume that their center frequencies are $\omega 1$ and $\omega 2$, respectively. In the case that $\omega 1 = \omega 2$, the interference phenomenon is the same as the HOM interference with narrow-band photons. In the case that $\omega 1 \neq \omega 2$, as shown in Fig. 1, the interference is equivalent to the HOM interference of a discrete frequency-entanglement state $(|\omega 1\rangle|\omega 2\rangle + |\omega 2\rangle|\omega 1\rangle)/\sqrt{2}$ because the occurrence of a coincidence count indicates two indistinguishable cases where one of the signal and idler photon is filtered by SFG1 and the other is filtered by SFG2 or vice versa. In the actual experiment, the SFG2 (or SFG1) module is not necessary to observe the beat note because once the signal or idler photon is filtered, the spectrum of the other photon is naturally selected by the coincidence measurement. Assuming the acceptance spectrum of the SFG1 and SFG2 has a Gaussian profile (the actual filtering profile is the sinc^2 function, which can be approximated as a Gaussian function), the coincidence detection probability is given by [15,21]

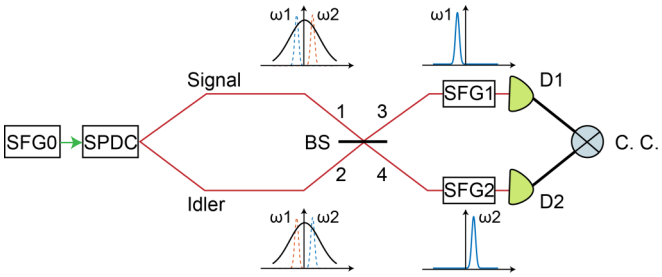

FIG. 1. A flow chart of the experimental setup. SPDC: spontaneous parametric down-conversion; BS: beam splitter; SFG: sum-frequency generation; D: single-photon detector; C. C.: coincidence count.

$$P = \tfrac{1}{2} - \tfrac{1}{2}\exp(-2\sigma^2\tau^2)\cos[(\omega_1 - \omega_2)\tau], \qquad (1)$$

where τ represents the time difference between signal and idler paths; σ represents the root mean square acceptance bandwidth of the two SFG systems.

Figure 2 shows the experimental setup. In the first SFG0 module, a type-0 periodically poled KTP crystal is used to generate the pump beam of SPDC that has a wavelength of 539.50 nm and maximum output power of 80 mW. In the experiment, the pump power is fixed at 38 mW. The 827.52 and 1549.92 nm pump beams are from a Ti:sapphire laser and an erbium-doped fiber amplifier, respectively. In the second system, a KTP crystal is used to implement the SPDC process. The *a*-cut KTP crystal can satisfy the type-II noncritical phase-matching condition around 1079 nm [29]. The degenerate temperature is 38 °C in our experiment. A polarizing beam splitter (PBS) is used to separate the signal and idler photons and the beam splitter (BS) in Fig. 1 is in fact realized using a fiber BS that is a 2×2 fiber coupler with a coupling ratio of nearly 50%/50%. The wave plates are used to translate the photons into the same polarization to satisfy the indistinguishability of the degree of freedom of polarization. SFG1 in Fig. 2(c) is a frequency up-conversion system where a type-0 MgO:PPLN crystal is used as the nonlinear crystal. The center frequency of the SFG acceptance spectrum can be tuned by adjusting the temperature of the crystal. The 1533.76 nm pump beam is from a diode laser and is amplified via another erbium-doped fiber amplifier that has a maximum output power of 10 W. The wavelength of the photons is converted to 633.40 nm. Another frequency up-conversion module SFG2 is cascaded together with SFG1. The pump beam in SFG2 is directly from SFG1; therefore,

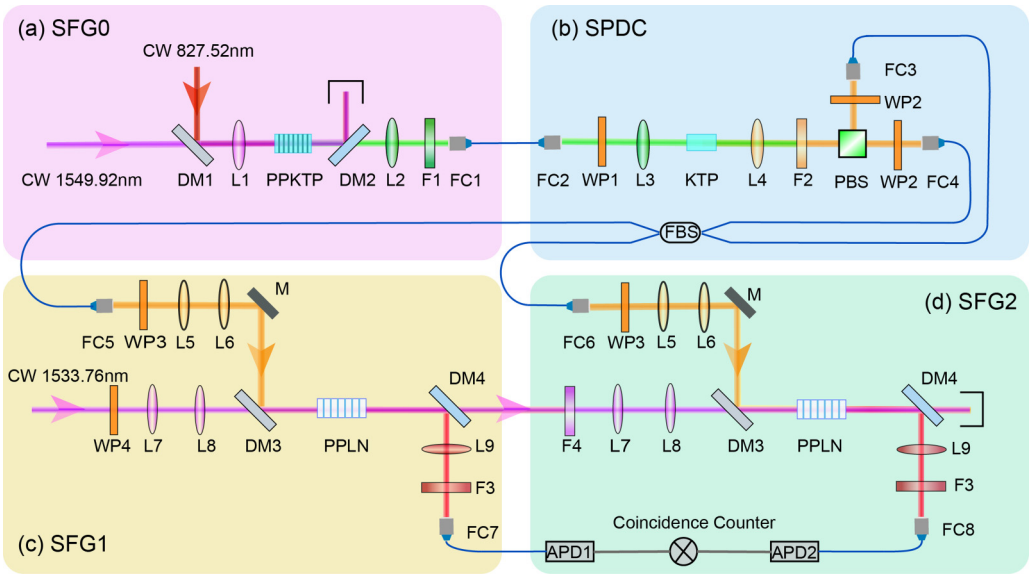

FIG. 2. Experimental setup. (a) SFG system preparing the pump beam of SPDC. PPKTP: periodically poled KTP crystal that has a poling period of 10.02 μm and a size of 20 mm (length) × 2 mm (width) × 1 mm (height); DM: dichroic mirror; F1: 520–40 nm band-pass filter; FC: fiber collimator. (b) SPDC system preparing photon pairs. WP: Wave plates including a quarter-wave plate and a half-wave plate; KTP: potassium titanyl phosphate crystal that has a size of 8 mm × 5 mm ×5 mm; PBS: polarizing beam splitter; F2: 750 nm long-pass filter; FBS: fiber beam spliter. (c,d) SFG systems realizing frequency up-conversion detection. PPLN:MgO-doped periodically poled lithium niobate crystal. The two PPLN crystals are identical that have five periodically poled gratings and each poled grating has a size of 40 mm × 1 mm × 0.5 mm. The period we used is 11.70 μm. F3: 635–10 nm band-pass filter; F4: 1400 nm long-pass filter. APD: Silicon avalanche photodiode (Excelitas, SPCM-AQRH-14-FC).

the pump power is lower than that in SFG1 because of the transmission loss of the optical elements. Except for the pump, the setup in SFG2 is identical to that in SFG1.

In SFG1 and SFG2, the pump beam and the photons from SPDC are focused by the lens group and have the focus size of the order of 50 and 40 μm, respectively. Figure 3(a) shows the net quantum conversion efficiency (QCE) data where the loss of the optical elements is excluded and the curves are fitted using the approximate linear function $\eta = kP$ and the function $\eta = \sin^2(\sqrt{\pi^2 P/4P_{\max}})$ [30] where P and $P_{\max}$ are the pump power and the power that maximizes the net QCE; $P_{\max 1} \approx$ 33W and $P_{\max 2} \approx$ 34W; k represents the approximate linear efficiency: $k_1 \approx k_2 \approx 6.2\%/\mathrm{W}$. Under our pump condition, the net QCEs of the two SFG systems are 56% and 50%, respectively. Given the loss of the optical elements and fiber coupling, the system QCEs are 25% and 20%, respectively. Figure 3(b) shows the acceptance spectra of the two SFG systems, which are fitted using the Gaussian function and the full width at half maximum (FWHM) acceptance bandwidths are both 0.2 nm. The center wavelength is dependent on the temperature. The temperatures corresponding to the two curves in Fig. 3(b) are 114.9 °C and 133.9 °C. Figure 3(c) shows the wavelength-temperature tuning curve of the two SFG modules. The proportional relations are 0.173 and 0.182 nm/°C for SFG1 and SFG2, respectively. The difference between the two curves is probably caused by the difference of the two thermistors in the temperature control systems. Although the same type of thermistor is used, they may have different nonlinear properties in the high-temperature range. Nevertheless, the tuning curves are measured, which provide an actual

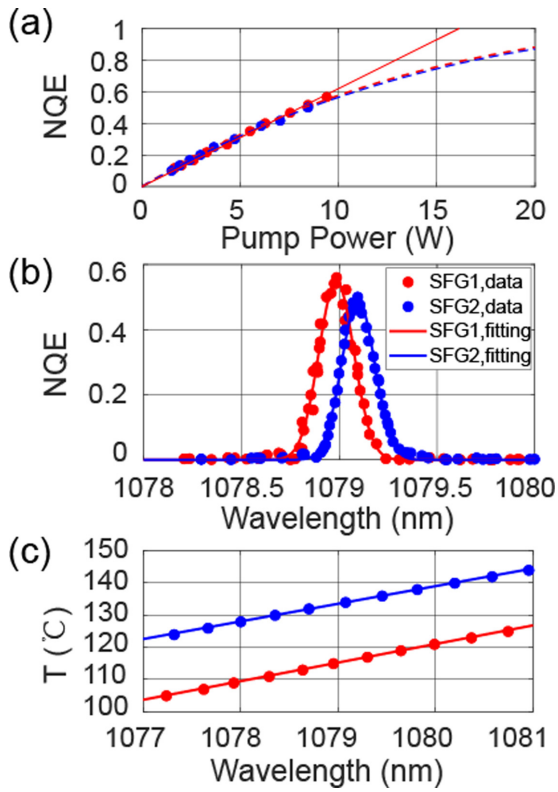

FIG. 3. (a) Net quantum conversion efficiency. (b) Acceptance spectra of the frequency up-conversion system SFG1 and SFG2. Corresponding temperatures are 114.9 °C and 133.9 °C, respectively. (c) Wavelength-temperature tuning curve of the two SFG systems.

TABLE I. Comparison between detections with and without SFG.

Type	Without SFG[a]	With SFG[b]
Signal and idler count N[c]	60 kHz ± 3 kHz	75 kHz ± 4 kHz
Coincidence count N_c	200 Hz ± 20 Hz	2600 Hz ± 80 Hz
Heralding efficiency $\eta_c = N_c/N$	0.33 ± 0.05%	3.47 ± 0.28%
Photons full bandwidth $\Delta\nu$[d]	0.75 THz (2.8 nm)	0.11 THz (0.4 nm)
Detector efficiency η_d[e]	< 2% (1079 nm)	68% (633 nm)

[a]FC3 and FC4 are linked with APD1 and APD2 using single-mode fiber, respectively.
[b]FC3 and FC4 are linked with FC5 and FC6 using single-mode fiber, respectively.
[c]To simplify the estimation, N represents the mean single-channel count of signal and idler photons $N = \sqrt{N_s N_i}$.
[d]The bandwidths without SFG are deduced from the fitting results in Fig. 4(a), while the bandwidth with SFG can be obtained from the results in Fig. 3(b) or 4(b).
[e]From the SPCM-AQRH data sheet [31].

temperature-wavelength mapping relation; therefore, the temperature difference shown in the following data can be directly transformed into the difference of the center acceptance wavelength.

III. RESULTS

To estimate the improvement of detection efficiency from frequency up-conversion, we measured the heralding efficiency with and without SFG systems and the experimental data are shown in Table I. Assuming subscripts 1 and 2 represent "without SFG" and "with SFG," the improvement of detection efficiency is given by $\kappa = \eta_{c2}/\eta_{c1} \approx 10.5$. The enhancement factor can also be approximately obtained from the single-channel count: $\kappa' = N_2\Delta\nu_1/N_1\Delta\nu_2 \approx 8.5$ where the filter effect of SFG should be considered. The smaller photon bandwidth after SFG makes the improvement of signal and idler count not as evident as the coincidence count. Considering the mean conversion efficiency $\eta = 22\%$, one can deduce the detector efficiency $\eta_{d1} = \eta\eta_{d2}/\kappa \approx 1.5\%$.

Although two SFG modules are included in Fig. 1, it is possible to observe the beat note with only one SFG module in one path and the photons in the other path are detected without SFG. Figure 4(a) shows the HOM interference result without SFG and Figs. 4(b)–4(e) show the results with single-path SFG where SFG1 is connected and SFG2 is skipped. Because the spectra of the signal and idler photon are the sinc^2 function, therefore the HOM-interference pattern should be a reversed triangle, while after being up-converted, the spectra of the photon pair will change from the sinc^2 function to the quasi-Gaussian function, and it will be well approximated by the Gaussian function [28]. Therefore, the envelopes of the data in Figs. 4(b)–4(e) are Gaussian forms and the data are fitted using Eq. (1). The coherence length of signal or idler photons is 0.4 mm which is obtained from the fitting result in Fig. 4(a) and the bandwidth can be calculated as 0.75 THz. The frequency differences obtained by fitting are (c) 0.176 THz; (d) 0.360 THz; (e) 0.530 THz. The predictive frequency differences are (c) 0.183 THz; (d) 0.366 THz; (e) 0.549 THz. The errors are from measurement errors, fitting errors, and the instability of the crystal temperature. Assuming C represents the count in the noninterference region and $C_{\min}$ represents the minimum count, the visibility is given by $V = (C - C_{\min})/C$. The visibilities from (a) to (e) are 94.13 ± 1.25%, 94.38 ± 1.42%, 97.47 ± 1.71%, 96.67 ± 2.27%, and 88.34 ± 3.29%, respectively. When we calculate the visibilities, the accidental coincidence counts are reduced. The data shown in Fig. 4(f) are the sum of the corresponding data in Figs. 4(b)–4(e). In principle, the sum of beat note data of all the entanglement frequency components should be equivalent to the HOM dip data in Fig. 4(a) because the HOM interference result is contributed by all the discrete frequency-entanglement components. The side peaks in Fig. 4(f) are caused by the inadequate summation where only four groups of data are summed. If more and denser data groups are measured and summed, the side peaks can vanish. The coherence length obtained by fitting the data in Fig. 4(f) is 0.48 mm. The error and imperfect dip are caused by the insufficient data.

Figures 4(g)–4(j) show the beat notes with double-path SFG, where (g) shows the HOM dip without frequency difference, and in other figures, the frequency differences obtained by fitting are (h) 0.192 THz; (i) 0.372 THz; (j) 0.553 THz; the predictive frequency differences are (h) 0.188 THz; (i) 0.376 THz; (j) 0. 564 THz. The bandwidth of the dip in Fig. 4(g) is slightly wider than that in Fig. 4(b). Two reasons contribute to this phenomenon: First, the spectral width of the double filter is naturally shorter than one filter [28] (the FWHM of function sinc^4 is slightly shorter than that of sinc^2); second, the imperfect superposition of the acceptance spectrum in Fig. 3(b) reduces the bandwidth of detectable frequency-entanglement photons. The advantage of two-path SFG is that the coincidence count can be significantly improved and the imperfect superposition of the two acceptance spectra is equivalent to a narrower bandwidth in a single-path SFG case, which can broaden the width of the beat note. The improvement of detection efficiency can also be reflected by the improvement of coincidence counts compared to those in the cases of single-path SFG or no SFG. These two points also improve the visibilities in the two-path SFG cases, even if the accidental coincidence counts are not reduced in these cases; the visibilities from (g) to (j) are 99.62 ± 0.12%, 99.21 ± 0.14%, 98.23 ± 0.18%, and 90.76 ± 1.10%, respectively. The visibility decreases with decreasing coincidence count and the decreasing count is due to the filtered spectrum shifting from the center to the boundary of the original photon spectrum of the SPDC.

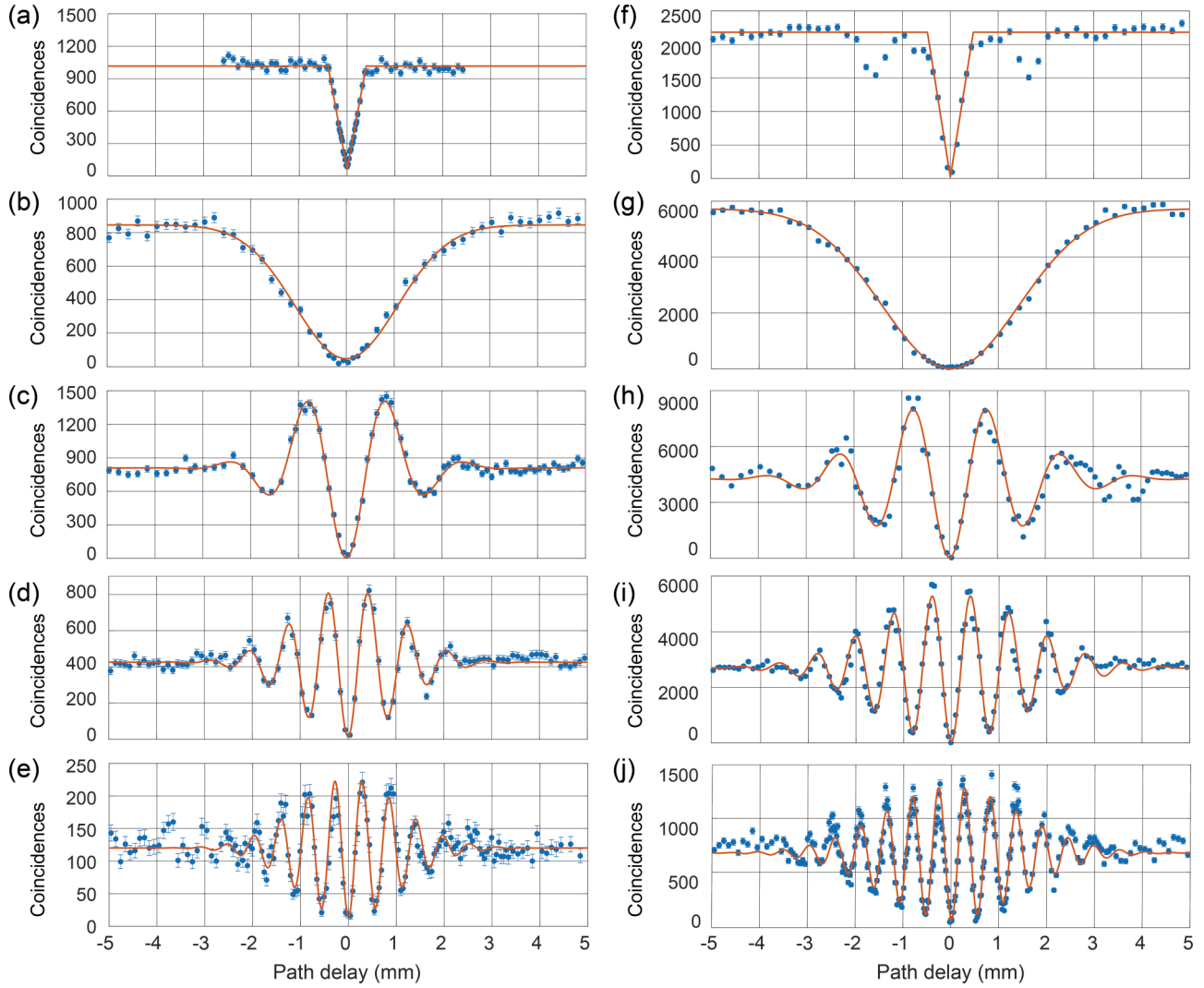

FIG. 4. HOM interference coincidence counts in 10 s (a) without SFG, (b)–(e) with single-path SFG, and (g)–(j) with two-path SFG. (f) The sum of the corresponding data in (b)–(e). Error bars are evaluated assuming the photon detection process obeys Poisson statistics. (a), (b), (g) are the HOM dip without frequency difference. In other panels, the frequency differences obtained by fitting are (c) 0.176 ± 0.002 THz (0.681 ± 0.007 nm); (d) 0.360 ± 0.004 THz (1.40 ± 0.014 nm); (e) 0.530 ± 0.011 THz (2.060 ± 0.041 nm); (h) 0.192 ± 0.003 THz (0.743± 0.012 nm); (i) 0.372 ± 0.002 THz (1.444± 0.008 nm); (j) 0.553 ± 0.004 THz (2.148 ± 0.015 nm). The predictive frequency differences are (c) 0.183 ± 0.005 THz (0.692 ± 0.017 nm); (d) 0.366 ± 0.005 THz (1.384 ± 0.017 nm); (e) 0.549 ± 0.005 THz (2.076 ± 0.017 nm); (h) 0.188± 0.009 THz (0.710 ± 0.036 nm); (i) 0.376± 0.009 THz (1.420 ± 0.036 nm); (j) 0. 564± 0.009 THz (2.130 ± 0.036 nm). The uncertainties are from fitting and the instability of temperature.

IV. DISCUSSION

In summary, we have shown three main advantages of NFC in quantum interference based on the HOM interferometer and the quantum spatial beating phenomenon. In the following, we further discuss these advantages.

Firstly, we look at preparing quantum states in different wave bands. Frequency conversion is always the main function of the NFC technique. Although the NFC has been used to prepare a short-wavelength quantum state in our previous work [28], here, we demonstrate this advantage from another aspect. The photon pair can be prepared using the noncritical phase-matching crystal, where the photon source could benefit from the large dimension of the crystal. Though the wavelength of the photons is limited to around 1079 nm, the NFC technique allows the photon pairs to be converted to any wave band without changing the correlation properties. In addition to the short wave, the 1079 nm photon can also be converted to the mid-IR band based on the DFG, which can extend the application scenarios of HOM interferometry.

Secondly, we note the improvement of the detection quality. In some application scenarios, the HOM interferometers should work in the IR band, for example, measurement of the refractive index, absorption, and dispersion of fibers or glasses in the IR band. Then, the visible detector with the aid of a high-efficiency SFG module can significantly improve the quality of infrared detection. Especially at present, there have been few reports of single-photon detectors in 2.3–5 μm with high quality and low cost, while in this wave band the NFC based on a PPLN crystal can still work. We demonstrate the

improvement of detection efficiency using the same silicon avalanche photodiode (APD) and SFG modules. Although the photon detectors based on AsGaIn and superconductivity have relatively high efficiency, they both require complex and costly cooling systems to reduce the noise. In our experiment, the net QCE is limited by the pump power, and the linear losses of some elements are not optimized; thus, total system QCE can be further optimized in the practical application scenarios. Besides, the PPLN waveguide may be a good candidate for NFC because of high QCE and low losses. Moreover, in our experiment the SFG modules do not introduce additional noise because the pump laser has a longer wavelength, the noise caused by scattering is far away from the detection band, and the noise caused by second- or high-harmonic generation can be easily filtered by the interference filters.

Finally, there is the filtering effect. We demonstrate that a NFC module can be used as a tunable narrow-band filter in a HOM interferometer, where the acceptance bandwidth is dependent on the length of the crystal. In our experiment, to tune the center frequency of the acceptance spectrum, the temperature of the crystal is adjusted, although adjustment of the pump wavelength is more convenient and fast. Compared with the common tunable filters that are based on gratings or prisms, the nonlinear filter cannot change the light path, which is a more stable system. Similar to a common narrow-band filter, the NFC can increase the coherence length and interference visibility. Besides, the NFC can also be used as an ideal polarizer; for example, the type-0 phase-matching condition can only work for the vertical polarization, which is also an important factor that can ensure the distinguishability of the polarization and improve the HOM interference visibility. The adjustability of the center frequency can not only help to optimize the sensitivity limits of the HOM interferometers [21] but can also be used as a spectrum analyzer. Based on this spectrum analyzer, we demonstrate that the HOM interference is the combined result of interference of all the frequency-entanglement components and the HOM dip is the combined result of all the corresponding beat notes. In other words, the results show that the beat notes are the fine structures of the HOM dip. In Fig. 1, the two filters played by the SFG modules after the BS are equivalent to two double filters before the BS. In this sense, the HOM interference with beat note phenomenon can be considered as a two-photon frequency-domain double-slit interference; the function of the HOM dip that is the envelope of the beat note is an analogy to the result of single-slit diffraction; the bandwidth of the filter is an analogy to the width of the slit.

Our results demonstrate the NFC could be a multifunctional auxiliary tool in the experiments of HOM interference. Moreover, these advantages can also be generalized to other quantum interference.

ACKNOWLEDGMENTS

This work is supported in part by National Natural Science Foundation of China (NSFC) (Grants No. 92065101 and No. 11934013), Anhui Initiative in Quantum Information Technologies (Grant No. AHY020200), and Space Debris Research Project of China (Grant No. KJSP2020020202).

[1] C. K. Hong, Z. Y. Ou, and L. Mandel, Phys. Rev. Lett. **59**, 2044 (1987).
[2] Y. H. Shih and C. O. Alley, Phys. Rev. Lett. **61**, 2921 (1988).
[3] C. Santori, D. Fattal, J. Vuckovic, G. S. Solomon, and Y. Yamamoto, Nature (London) **419**, 594 (2002).
[4] V. Giovannetti, S. Lloyd, and L. Maccone, Science **306**, 1330 (2004).
[5] J.-H. Kim, T. Cai, C. J. K. Richardson, R. P. Leavitt, and E. Waks, Optica **3**, 577 (2016).
[6] Y. Zhang, F. S. Roux, T. Konrad, M. Agnew, J. Leach, and A. Forbes, Sci. Adv. **2**, e1501165 (2016).
[7] F. Bouchard, A. Sit, Y. Zhang, R. Fickler, F. M. Miatto, Y. Yao, F. Sciarrino, and E. Karimi, Rep. Prog. Phys. **84**, 012402 (2021).
[8] A. Lyons, G. C. Knee, E. Bolduc, T. Roger, J. Leach, E. M. Gauger, and D. Faccio, Sci. Adv. **4**, eaap9416 (2018).
[9] M. B. Nasr, B. E. A. Saleh, A. V. Sergienko, and M. C. Teich, Phys. Rev. Lett. **91**, 083601 (2003).
[10] A. M. Steinberg, P. G. Kwiat, and R. Y. Chiao, Phys. Rev. Lett. **68**, 2421 (1992).
[11] Y.-R. Fan, C.-Z. Yuan, R.-M. Zhang, S. Shen, P. Wu, H.-Q. Wang, H. Li, G.-W. Deng, H.-Z. Song, L.-X. You, Z. Wang, Y. Wang, G.-C. Guo, and Q. Zhou, Photonics Res. **9**, 1134 (2021).
[12] Z.-Y. Zhou, D.-S. Ding, B.-S. Shi, X.-B. Zou, and G.-C. Guo, Phys. Rev. A **85**, 023841 (2012).
[13] D. Branning, A. L. Migdall, and A. V. Sergienko, Phys. Rev. A **62**, 063808 (2000).
[14] R. Okamoto, S. Takeuchi, and K. Sasaki, Phys. Rev. A **74**, 011801(R) (2006).
[15] Z. Y. Ou and L. Mandel, Phys. Rev. Lett. **61**, 54 (1988).
[16] S. Ramelow, L. Ratschbacher, A. Fedrizzi, N. K. Langford, and A. Zeilinger, Phys. Rev. Lett. **103**, 253601 (2009).
[17] Z. C. Zhang, C. Z. Yuan, S. Shen, H. Yu, R. M. Zhang, H. Q. Wang, H. Li, Y. Wang, G. W. Deng, Z. M. Wang, L. X. You, Z. Wang, H. Z. Song, G. C. Guo, and Q. Zhou, npj Quantum Inf. **7**, 123 (2021).
[18] Q. Zhou, W. Zhang, C. Yuan, Y. Huang, and J. Peng, Opt. Lett. **39**, 2109 (2014).
[19] Q. Zhou, S. Dong, W. Zhang, L. You, Y. He, W. Zhang, Y. Huang, and J. Peng, J. Opt. Soc. Am. B **31**, 1801 (2014).
[20] F. Kaneda, H. Suzuki, R. Shimizu, and K. Edamatsu, Opt. Express **27**, 1416 (2019).
[21] Y. Chen, M. Fink, F. Steinlechner, J. P. Torres, and R. Ursin, npj Quantum Inf. **5**, 43 (2019).
[22] S. Tanzilli, W. Tittel, M. Halder, O. Alibart, P. Baldi, N. Gisin, and H. Zbinden, Nature (London) **437**, 116 (2005).
[23] Z. Y. Zhou, Y. Li, D. S. Ding, W. Zhang, S. Shi, B. S. Shi, and G. C. Guo, Light Sci. Appl. **5**, e16019 (2016).
[24] T. Nagata, R. Okamoto, L. O'Brien J, K. Sasaki, and S. Takeuchi, Science **316**, 726 (2007).

[25] J. S. Dam, P. Tidemand-Lichtenberg, and C. Pedersen, Nat. Photonics **6**, 788 (2012).
[26] B. Dayan, A. Pe'er, A. A. Friesem, and Y. Silberberg, Phys. Rev. Lett. **94**, 043602 (2005).
[27] T. B. Pittman, Y. H. Shih, D. V. Strekalov, and A. V. Sergienko, Phys. Rev. A **52**, R3429(R) (1995).
[28] Z.-Y. Zhou, S.-L. Liu, S.-K. Liu, Y.-H. Li, D.-S. Ding, G.-C. Guo, and B.-S. Shi, Phys. Rev. Appl. **7**, 064025 (2017).
[29] Z. Y. Ou, S. F. Pereira, E. S. Polzik, and H. J. Kimble, Opt. Lett. **17**, 640 (1992).
[30] M. A. Albota and F. N. Wong, Opt. Lett. **29**, 1449 (2004).
[31] https://www.excelitas.com/product/spcm-aqrh.